Superconvergence and H(div) Projection for Discontinuous Galerkin Methods

Peter Bastian [1] *and Béatrice Rivière [2]

[1] *Interdisziplinäres Zentrum für Wissenschaftliches Rechnen, Universität Heidelberg,*
Im Neuenheimer Feld 348, 69120 Heidelberg, Germany
[2] *Department of Mathematics, 301 Thackeray, University of Pittsburgh, Pittsburgh, PA 15260, USA*

SUMMARY

We introduce and analyze a projection of the discontinuous Galerkin (DG) velocity approximations that preserve the local mass conservation property. The projected velocities have the additional property of continuous normal component. Both theoretical and numerical convergence rates are obtained which show that the accuracy of the DG velocity field is maintained. Superconvergence properties of the DG methods are shown. Finally, numerical simulations of complicated flow and transport problem illustrate the benefits of the projection. Copyright © 2000 John Wiley & Sons, Ltd.

KEY WORDS: locally conservative projection, superconvergence of fluxes, error estimates, flow, transport

1. Introduction

The objective of this paper is to study the effects of the discontinuities in the fluxes of the discontinuous Galerkin approximations of elliptic problems. Due to their flexibility, discontinuous Galerkin (DG) methods have been popular among the finite element community and they have been applied to a wide range of computational fluid problems. Since the first DG method introduced in [16] the methods have been developed for hyperbolic problems, see [7] for an overview, and for elliptic problems in [21, 15, 8, 17, 18, 11]. A unified analysis for many DG methods has been given recently in [4].

Advantages of DG methods are their higher order convergence property, local conservation of mass and flexibility with respect to meshing and *hp*-adaptive refinement. Their uniform applicability to hyperbolic, elliptic and parabolic problems as well as their robustness with

respect to strongly discontinuous coefficients renders them very attractive for porous medium flow and transport calculations [20, 2]. One disadvantage is, however, that the normal component of the velocity field is not continuous at inter-element boundaries. This leads to non-physical oscillations if a DG flow calculation is coupled to a DG transport calculation in a straightforward way. Moreover, the sign of the normal fluxes may be different from both sides of an edge (or face in 3D) which makes it impossible to do particle tracking or to employ the flow field in connection with characteristic type methods.

In this paper we present a simple and cheap postprocessing technique for the DG velocity field that results in continuous normal component at inter-element boundaries. In principle any finite element space contained in $H(\mathrm{div})$ can be used for this postprocessing. We have chosen the BDM finite element spaces introduced in [5] because they nicely match in dimension with the space of velocities generated by the DG method. It is shown that the postprocessed velocity field has the following properties:

1. The new velocity field identically reproduces the averaged normal flux of the DG velocity field. This is important because averaged normal fluxes in the DG method are locally conservative.
2. The new velocity field has continuous normal component at inter-element boundaries.
3. It has the same accuracy and order of convergence as the original DG velocity field.

The normal flux at inter-element boundaries plays an important role in the construction of the projected velocity field. As a side effect we show numerically that those fluxes and the jumps of pressure in the DG method are superconvergent by one order if the problem possesses enough regularity.

The paper is organized as follows. In Section 2 we state the continuous problem, its DG discretization and introduce the necessary notation. Section 3 describes the construction of the locally conservative velocity projection scheme and the next section presents several error estimates. Section 5 contains the numerical results and some conclusions are given in the last Section.

2. Model Problem and Scheme

Let Ω be a polygonal domain in $\mathbb{R}^n, n = 2, 3$. Let the boundary of the domain $\partial\Omega$ be the union of two disjoint sets Γ_D and Γ_N. For $f \in L^2(\Omega), p_0 \in H^{1/2}(\Gamma_D)$ and $g \in L^2(\Gamma_N)$, we consider the following elliptic problem:

$$\nabla \cdot \boldsymbol{u} = f, \quad \text{in} \quad \Omega, \tag{1}$$

$$\boldsymbol{u} = -\boldsymbol{K}\nabla p, \quad \text{in} \quad \Omega, \tag{2}$$

$$p = p_0, \quad \text{on} \quad \Gamma_D, \tag{3}$$

$$\boldsymbol{u} \cdot \boldsymbol{n} = g, \quad \text{on} \quad \Gamma_N. \tag{4}$$

Here, $\boldsymbol{K}$ is a symmetric positive definite matrix and $\boldsymbol{n}$ is the outward normal vector to $\partial\Omega$.

In groundwater applications, the problem (1)-(4) characterizes the single phase flow in a porous medium with p the fluid pressure, $\boldsymbol{u}$ the Darcy velocity and $\boldsymbol{K}$ the permeability field. It is essential to develop numerical schemes that yield very accurate approximations of the

velocity. The velocity obtained in (1)-(4) contributes to the advection of the solute transport problem described below:

$$\psi\frac{\partial S}{\partial t} + \nabla \cdot (S\boldsymbol{u} - D\nabla S) = R(S), \quad \text{in} \quad \Omega, \tag{5}$$

$$(S\boldsymbol{u} - D\nabla S) \cdot \boldsymbol{n} = S_{\text{in}}\boldsymbol{u} \cdot \boldsymbol{n}, \quad \text{on} \quad \Gamma_+, \tag{6}$$

$$D\nabla S \cdot \boldsymbol{n} = 0, \quad \text{on} \quad \Gamma_-, \tag{7}$$

where S is the saturation of the species advected, ψ the porosity of the porous medium, D the molecular diffusion-dispersion coefficient, $R(S)$ a general reaction-source term and Γ_+ (resp. Γ_-) the inflow (resp. outflow) boundary.

$$\Gamma_+ = \{x \in \partial\Omega : \boldsymbol{u} \cdot \boldsymbol{n} > 0\}, \quad \Gamma_- = \partial\Omega \setminus \Gamma_+.$$

Let $\mathcal{E}_h = \{E\}_E$ be a non-degenerate quasi-uniform subdivision of Ω, where E is a triangle or a quadrilateral if $n = 2$, or a tetrahedron or hexaedron if $n = 3$. Let h denote the maximum diameter of the elements in $\mathcal{E}_h$. The set of all interior and Dirichlet edges (or faces) is denoted by Γ_h. With each edge (or face) e, we associate a unit normal vector $\boldsymbol{n}_e$. For a boundary edge e, $\boldsymbol{n}_e$ is taken to be the unit outward normal vector. For real $m \geq 0$ define,

$$H^m(\mathcal{E}_h) = \{w \in L^2(\Omega) : w|_E \in H^m(E) \; \forall E \in \mathcal{E}_h\}$$

The usual Sobolev norm of H^m on $E \subset \mathbb{R}^n$ is denoted by $\| \cdot \|_{m,E}$. The reader can refer to Adams [1] and to Lions and Magenes [13] for the properties of Sobolev spaces. We define the following broken norms for positive integer m and for $w \in H^m(\mathcal{E}_h)$:

$$\|w\|_m = \left(\sum_{E \in \mathcal{E}_h} \|w\|_{m,E}^2\right)^{\frac{1}{2}}.$$

We now define the average and the jump for $w \in H^m(\mathcal{E}_h)$, $m > \frac{1}{2}$. We assume that $\boldsymbol{n}_e$ is exterior to E_e^1.

$$\{w\} = \tfrac{1}{2}(w|_{E_e^1}) + \tfrac{1}{2}(w|_{E_e^2}), \quad [w] = (w|_{E_e^1}) - (w|_{E_e^2}), \quad \forall e = \partial E_e^1 \cap \partial E_e^2,$$
$$\{w\} = w|_{E_e^1}, \qquad\qquad [w] = w|_{E_e^1}, \quad \forall e = \partial E_e^1 \cap \partial\Omega.$$

The finite element subspaces consist of discontinuous piecewise polynomials:

$$\mathcal{D}_k = \{w : w|_E \in \mathbb{P}_k(E) \quad \forall E \in \mathcal{E}_h\},$$

where $\mathbb{P}_k(E)$ is a discrete space containing the set of polynomials of total degree less than or equal to k on E. We now present the discontinuous Galerkin scheme for solving the elliptic problem (1)-(4): find $P^{\text{DG}} \in \mathcal{D}_k$ such that

$$\sum_E \int_E \boldsymbol{K}\nabla P^{\text{DG}} \cdot \nabla w - \sum_{e \in \Gamma_h} \int_e \{\boldsymbol{K}\nabla P^{\text{DG}} \cdot \boldsymbol{n}_e\}[w] + \sum_{e \in \Gamma_h} \int_e \{\boldsymbol{K}\nabla w \cdot \boldsymbol{n}_e\}[P^{\text{DG}}]$$
$$= \int_\Omega fw + \sum_{e \in \Gamma_D} \int_e \boldsymbol{K}\nabla w \cdot \boldsymbol{n}_e p_0 - \sum_{e \in \Gamma_N} \int_e gw, \quad \forall w \in \mathcal{D}_k. \tag{8}$$

Let $\boldsymbol{U}^{\text{DG}}$ denote the DG velocity obtained as follows:

$$\boldsymbol{U}^{\text{DG}} = -\boldsymbol{K}\nabla P^{\text{DG}}. \tag{9}$$

We easily see that the DG velocity satisfies the conservation of mass locally on each element E with $\boldsymbol{n}_E$ the outward normal to ∂E:

$$\int_{\partial E} \{\boldsymbol{U}^{\mathrm{DG}} \cdot \boldsymbol{n}_E\} = \int_E f, \quad \forall E \in \mathcal{E}_h.$$

This property of the DG approximations is an appealing feature. However, the pointwise discontinuity in the normal component of the DG velocity produces an additional numerical error that can be significant in applications where transport is coupled to non-uniform flow. We address this problem by defining a H(div) projection of the DG velocity, described below.

3. A locally conservative projection

In this section, we present a local projection on each element of the subdivision, from the space of totally discontinuous velocities to the space of velocities that have continuous normal components. The resulting velocity lies in the velocity subspace of the BDM spaces [5] introduced by Brezzi, Douglas and Marini. The construction of the projection is as follows: fix an element E with edges $e_i, i = 1, 2, 3$ and let $\boldsymbol{U}^* \in (\mathbb{P}_{k-1}(E))^2$ be such that

$$\int_{e_i} (\boldsymbol{U}^* \cdot \boldsymbol{n}_{e_i})z = \int_{e_i} (\{\boldsymbol{U}^{\mathrm{DG}}\} \cdot \boldsymbol{n}_{e_i})z, \quad \forall z \in \mathbb{P}_{k-1}(e_i), \quad i = 1, 2, 3, \tag{10}$$

$$\int_E \boldsymbol{U}^* \cdot \nabla w = \int_E \boldsymbol{U}^{\mathrm{DG}} \cdot \nabla w, \quad \forall w \in \mathbb{P}_{k-2}(E), \tag{11}$$

$$\int_E \boldsymbol{U}^* \cdot \mathbf{S}(\phi) = \int_E \boldsymbol{U}^{\mathrm{DG}} \mathbf{S}(\phi), \quad \forall \phi \in M_k(E). \tag{12}$$

Here, $\mathbf{S}(\phi) = (\frac{\partial \phi}{\partial x_2}, -\frac{\partial \phi}{\partial x_1})$ and the space $M_k(E)$ is the finite dimensional space of polynomials vanishing on the boundary of E.

$$M_k(E) = \{\phi \in \mathbb{P}_k(E) : \phi|_{\partial E} = 0\}.$$

One interesting characteristic of our construction is that the H(div) projection defined in [5] is applied to the *average* of the DG fluxes.

Lemma 3.1. *The conditions (10), (11) and (12) uniquely define $\boldsymbol{U}^*$.*

Proof: Since the system defining $\boldsymbol{U}^*$ is of finite dimension, it suffices to show uniqueness of $\boldsymbol{U}^*$. It is equivalent to prove that if $\boldsymbol{v} \in (\mathbb{P}_{k-1}(E))^2$ satisfies

$$\int_{e_i} (\boldsymbol{v} \cdot \boldsymbol{n}_{e_i})z = 0, \quad \forall z \in \mathbb{P}_{k-1}(e_i), \quad i = 1, 2, 3, \tag{13}$$

$$\int_E \boldsymbol{v} \cdot \nabla w = 0, \quad \forall w \in \mathbb{P}_{k-2}(E), \tag{14}$$

$$\int_E \boldsymbol{v} \cdot \mathbf{S}(\phi) = 0, \quad \forall \phi \in M_k(E). \tag{15}$$

then, $\boldsymbol{v}$ vanishes. Clearly, the first conditions imply that $\boldsymbol{v} \cdot \boldsymbol{n}_{e_i} = 0$ for $i = 1, 2, 3$. In the case where $k = 2$, this immediately implies that $\boldsymbol{v} = 0$. We also have

$$\int_E \nabla \cdot \boldsymbol{v} \nabla \cdot \boldsymbol{v} = -\int_E \boldsymbol{v} \cdot \nabla(\nabla \cdot \boldsymbol{v}) + \int_{\partial E} \boldsymbol{v} \cdot \boldsymbol{n}_E \nabla \cdot \boldsymbol{v}.$$

Copyright © 2000 John Wiley & Sons, Ltd.
Prepared using fldauth.cls

Int. J. Numer. Meth. Fluids 2000; **00**:1–6

Since $\nabla \cdot \boldsymbol{v} \in I\!P_{k-2}(E)$, the condition (14) yields

$$\int_E \nabla \cdot \boldsymbol{v}\nabla \cdot \boldsymbol{v} = 0,$$

thus $\nabla \cdot \boldsymbol{v} = 0$. Therefore, there is a function $\phi \in I\!P_k(E)$ such that $\boldsymbol{v} = \mathbf{S}(\phi)$. An easy computation gives $\nabla\phi \cdot \boldsymbol{t} = \boldsymbol{v} \cdot \boldsymbol{n} = 0$, with $\boldsymbol{t}$ the unit tangential vector along ∂E. Thus, we can take ϕ in $M_k(E)$ and we have by (15)

$$\|\boldsymbol{v}\|_{0,E}^2 = \int_E \boldsymbol{v} \cdot \mathbf{S}(\phi) = 0.$$

Thus, $\boldsymbol{v} = 0$, which concludes the proof.

We note that the new velocity $\boldsymbol{U}^*$ has both advantages of a continuous normal component and a local mass conservation:

$$\int_{\partial E} \boldsymbol{U}^* \cdot \boldsymbol{n}_E = \int_E f, \quad \forall E \in \mathcal{E}_h.$$

4. Error estimates

It is well known [18] that if the solution p of (1)-(4) belongs to $H^s(\mathcal{E}_h)$, for $s \geq 2$, then there is a constant C independent of h and k such that

$$\|\boldsymbol{U}^{\mathrm{DG}} - \boldsymbol{u}\|_0 \leq C\frac{h^{\min(k+1,s)-1}}{k^{s-\frac{5}{2}}}\|p\|_s. \tag{16}$$

In this section, our main result shows that the convergence rate for the error in the projected velocities is optimal with respect to the mesh size. We first recall a trace theorem [3], an inverse estimate and the DG interpolant [18] needed for proving the estimates.

Lemma 4.1. *Let E be an element of $\mathcal{E}_h$.*

$$\|\nabla\xi \cdot \boldsymbol{n}_e\|_{0,e}^2 \leq C(h^{-1}\|\nabla\xi\|_{0,E}^2 + h\|\nabla^2\xi\|_{0,E}^2), \quad \forall e \subset \partial E, \quad \forall \xi \in H^2(E), \tag{17}$$

$$\|\nabla\xi \cdot \boldsymbol{n}_e\|_{0,e}^2 \leq Ck^2 h^{-1}\|\nabla\xi\|_{0,E}^2, \quad \forall e \subset \partial E, \quad \forall \xi \in I\!P_k(E). \tag{18}$$

Lemma 4.2. *Let $p \in H^s(\mathcal{E}_h)$ with $s \geq 2$ be the solution of (1)-(4). Let $k \geq 2$. There is an interpolant $P^{\mathrm{I}} \in \mathcal{D}_k$ of p such that:*

$$\|\nabla^i(p - P^{\mathrm{I}})\|_0 \leq C\frac{h^{min(k+1,s)-i}}{k^{s-3/2-\delta}}\|p\|_s, \quad i = 0, 1, 2, \tag{19}$$

where $\delta = 0$ if $i = 0, 1$ and $\delta = 0.5$ if $i = 2$, and C is a constant independent of h and k. Besides, we have

$$\|\nabla(P^{\mathrm{DG}} - P^{\mathrm{I}})\|_0 \leq C\frac{h^{\min(k+1,s)-1}}{k^{s-\frac{5}{2}}}\|p\|_s. \tag{20}$$

We analyze the error in the normal components of the DG velocities.

Lemma 4.3. *Let $(p, \boldsymbol{u})$ be solution of (1)-(4) such that $p \in H^s(\mathcal{E}_h)$ for $s \geq 2$. Let $\boldsymbol{U}^{\mathrm{DG}}$ be defined by (9). Then, we have for any element E of $\mathcal{E}_h$*

$$\|(\{\boldsymbol{U}^{\mathrm{DG}}\} - \boldsymbol{u}) \cdot \boldsymbol{n}_e\|_{0,e} \leq C\frac{h^{\min(k+1,s)-3/2}}{k^{s-\frac{7}{2}}}\|p\|_s, \quad \forall e \subset \partial E.$$

Proof: Let $\boldsymbol{U}^{\mathrm{I}} = -K\nabla P^{\mathrm{I}}$ with P^{I} defined in Lemma 4.2. Then, we have

$$\|\{\boldsymbol{U}^{\mathrm{DG}}\} - \boldsymbol{u}\|_{0,e} \leq \|(\{\boldsymbol{U}^{\mathrm{DG}}\} - \{\boldsymbol{U}^{\mathrm{I}}\}) \cdot \boldsymbol{n}_e\|_{0,e} + \|(\{\boldsymbol{U}^{\mathrm{I}}\} - \boldsymbol{u}) \cdot \boldsymbol{n}_e\|_{0,e}.$$

By the inverse estimate (18) and the bound (20), we obtain

$$\|(\{\boldsymbol{U}^{\mathrm{DG}}\} - \{\boldsymbol{U}^{\mathrm{I}}\}) \cdot \boldsymbol{n}_e\|_{0,e} \leq Ckh^{-1/2}\|K\nabla(P^{\mathrm{DG}} - P^{\mathrm{I}})\|_{\mathcal{S}(e)}$$
$$\leq C\frac{h^{\min(k+1,s)-3/2}}{k^{s-\frac{7}{2}}}\|p\|_s.$$

Here, $\mathcal{S}(e)$ denotes the set of elements of $\mathcal{E}_h$ that share the edge e. By the trace theorem (17) and the approximation result (19):

$$\|(\{\boldsymbol{U}^{\mathrm{I}}\} - \boldsymbol{u}) \cdot \boldsymbol{n}_e\|_{0,e} \leq C(h^{-1/2}\|\nabla(P^{\mathrm{I}} - p)\|_{0,\mathcal{S}(e)} + h^{1/2}\|\nabla^2(P^{\mathrm{I}} - p)\|_{0,\mathcal{S}(e)})$$
$$\leq C\frac{h^{\min(k+1,s)-3/2}}{k^{s-2}}\|p\|_s.$$

The final result is obtained by combining the two bounds.

Remark: By construction of $\boldsymbol{U}^*$, Lemma 4.3 immediately implies

$$\|(\boldsymbol{U}^* - \boldsymbol{u}) \cdot \boldsymbol{n}_e\|_{0,e} \leq C\frac{h^{\min(k+1,s)-3/2}}{k^{s-\frac{7}{2}}}\|p\|_s, \quad \forall e \subset \partial E.$$

Lemma 4.4. *Let p be the solution of (1)-(4) such that $p \in H^s(\mathcal{E}_h)$ for $s \geq 2$. Let $(P^{\mathrm{DG}}, \boldsymbol{U}^{\mathrm{DG}})$ be defined by (8) and (9). Then, we have for each element $E \in \mathcal{E}_h$*

$$\|[P^{\mathrm{DG}}]\|_{0,e} + \|[\boldsymbol{U}^{\mathrm{DG}}] \cdot \boldsymbol{n}_e\|_{0,e} \leq C\frac{h^{\min(k+1,s)-3/2}}{k^{s-\frac{7}{2}}}\|p\|_s, \quad \forall e \in \partial E.$$

Proof: We note that

$$\|[P^{\mathrm{DG}}]\|_{0,e} = \|[P^{\mathrm{DG}} - p]\|_{0,e}, \quad \|[\boldsymbol{U}^{\mathrm{DG}}] \cdot \boldsymbol{n}_e\|_{0,e} = \|[\boldsymbol{U}^{\mathrm{DG}} - \boldsymbol{u}] \cdot \boldsymbol{n}_e\|_{0,e},$$

and we apply similar techniques as in Lemma 4.3.

Theorem 4.5. *For any element E of the subdivision $\mathcal{E}_h$, there is a constant C independent of h such that*

$$\|\boldsymbol{U}^* - \boldsymbol{U}^{\mathrm{DG}}\|_{0,E} \leq Ch^{\min(k+1,s)-1}\|p\|_s,$$

Proof: Let us fix an element E of $\mathcal{E}_h$ and let us denote by $n(e_i; E)$ the element of $\mathcal{E}_h$ that is a neighbor of E via the edge $e_i \subset \partial E$. Let us define $\boldsymbol{\chi} = \boldsymbol{U}^* - \boldsymbol{U}^{\mathrm{DG}}$. Then, from (10)-(12), $\boldsymbol{\chi}$ satisfies:

$$\int_{e_i}(\boldsymbol{\chi} \cdot \boldsymbol{n}_{e_i})z = -\frac{1}{2}\int_{e_i}(\boldsymbol{U}^{\mathrm{DG}}|_E - \boldsymbol{U}^{\mathrm{DG}}|_{n(e_i;E)}) \cdot \boldsymbol{n}_{e_i}, \quad \forall z \in \mathbb{P}_{k-1}(e_i), \quad i = 1, 2, 3,$$

$$\int_E \boldsymbol{\chi} \cdot \nabla w = 0, \quad \forall w \in \mathbb{P}_{k-2}(E),$$

$$\int_E \boldsymbol{\chi} \cdot \mathbf{S}(\phi) = 0, \quad \forall \phi \in M_k(E).$$

The first equation clearly implies that $\boldsymbol{\chi}|_{\partial E} = -\frac{1}{2}(\boldsymbol{U}^{\mathrm{DG}}|_E - \boldsymbol{U}^{\mathrm{DG}}|_{n(e_i;E)})|_{\partial E}$. Passing to the reference element $\hat{E}$, we have $\|\boldsymbol{\chi}\|_{0,E} \le Ch\|\hat{\boldsymbol{\chi}}\|_{0,\hat{E}}$. We now show that $\|\cdot\|_{0,\partial\hat{E}}$ is a norm for the discrete space

$$\{\boldsymbol{v} \in (I\!\!P_{k-1}(\hat{E}))^2 : \int_{\hat{E}} \boldsymbol{v} \cdot \nabla w = 0 \quad \forall w \in I\!\!P_{k-2}(\hat{E}), \quad \int_{\hat{E}} \boldsymbol{v} \cdot \mathbf{S}(\phi) = 0 \quad \forall \phi \in M_k(\hat{E})\}.$$

It suffices to show that if $\boldsymbol{v}$ vanishes on $\partial\hat{E}$, then $\boldsymbol{v}$ vanishes on $\hat{E}$. This follows from the proof of the uniqueness of the H(div) projection of Lemma 3.1. Thus, we have

$$\|\boldsymbol{\chi}\|_{0,E} \le Ch\|\hat{\boldsymbol{\chi}}\|_{0,\partial\hat{E}} \le Ch^{1/2}\|\boldsymbol{\chi}\|_{0,\partial E} \le Ch^{1/2}\|[\boldsymbol{U}^{\mathrm{DG}}]\|_{0,\partial E}.$$

The final result is then obtained from Lemma 4.4.

5. Numerical Experiments

5.1. Convergence studies

Smooth problem: In the first example we solve $-\Delta p = f$, $p = p_0$ on $\partial\Omega$, in the unit square $\Omega = (0,1)^2$ where f and p_0 are chosen such that the exact solution $p(x,y) = e^{-\left((x-1/2)^2+(y-1/2)^2\right)}$ is obtained. Table I lists the L^2-norm of the error in the DG velocity, in the new projected velocity and the difference of DG and projected velocity for $k = 2$ and $k = 3$. The experiments are run on quadrilateral and triangular meshes. As can be seen, all three differences converge with the same optimal rate k predicted by our theoretical results. Table II shows that fluxes and jumps of pressure at interior edges in the DG solution are superconvergent. The unstructured mesh is generated by a triangular mesh generator with $h \approx 1/4$. Finer meshes are obtained by regular refinement.

We note that the fluxes are superconvergent of order $O(h^{k+1/2})$ instead of $O(h^{k-1/2})$ as expected and the jumps of pressure are superconvergent of order $O(h^{k+3/2})$ instead of $O(h^{k+1/2})$. The latter is a very interesting result since it is known that numerically the error in the L^2 norm for the DG pressure is not optimal for even order polynomials. The best theoretical result so far is a rate of $O(h^{k-1/2})$. Here, superconvergence results are obtained for both odd and even polynomials.

Reentrant corner problem: In order to illustrate the dependence of the convergence on the regularity of the problem we solve $-\Delta p = 0$, $p = p_0$ on $\partial\Omega$ in a domain with a reentrant corner, in this case 7/8th of a circle. Dirichlet boundary conditions are taken from the exact solution $p(r,\phi) = r^{\frac{4}{7}}\sin(\frac{4}{7}\theta)$ in polar coordinates. The solution is in $H^s(\Omega)$ with $s = 1 + 4/7$. The theoretical convergence rate is now $s - 1 = 4/7 \approx 0.5714$ for the L^2 norm of the error in the velocities. This result is confirmed in Table III and as expected, the convergence rate is independent of the polynomial degree. The convergence rate of fluxes at interior edges is $s - 3/2 = 1/14$ and the convergence rate of pressure jumps at interior edges is $s - 1/2 = 1 + 1/14$ as is fully confirmed in Table IV.

We also observe that the quantity $\boldsymbol{U}^{\mathrm{DG}} - \boldsymbol{U}^*$ can be used as an error indicator: it is easily obtained, computationally cheap and it does not require the knowledge of the exact solution. In the case of non-smooth solution, the convergence rate of the L^2 norm of $\boldsymbol{U}^{\mathrm{DG}} - \boldsymbol{U}^*$ is also a good indicator of the regularity of the solution.

Table I. Full regularity model problem.

h^{-1}	$\|\boldsymbol{U}^{\mathrm{DG}} - \boldsymbol{u}\|_0$	rate	$\|\boldsymbol{U}^* - \boldsymbol{u}\|_0$	rate	$\|\boldsymbol{U}^{\mathrm{DG}} - \boldsymbol{U}^*\|_0$	rate
		equidistant triangular mesh, $k = 2$				
8	$2.92 \cdot 10^{-3}$		$4.84 \cdot 10^{-3}$		$4.61 \cdot 10^{-3}$	
16	$7.30 \cdot 10^{-4}$	2.00	$1.22 \cdot 10^{-3}$	1.99	$1.16 \cdot 10^{-3}$	1.99
32	$1.82 \cdot 10^{-4}$	2.01	$3.05 \cdot 10^{-4}$	2.00	$2.90 \cdot 10^{-4}$	2.00
64	$4.55 \cdot 10^{-5}$	2.00	$7.62 \cdot 10^{-5}$	2.00	$7.26 \cdot 10^{-5}$	1.99
128	$1.14 \cdot 10^{-5}$	2.00	$1.91 \cdot 10^{-5}$	2.00	$1.82 \cdot 10^{-5}$	2.00
256	$2.84 \cdot 10^{-6}$	2.01	$4.76 \cdot 10^{-6}$	2.00	$4.54 \cdot 10^{-6}$	2.00
		equidistant quadrilateral mesh, $k = 2$				
8	$5.52 \cdot 10^{-3}$		$5.53 \cdot 10^{-3}$		$2.01 \cdot 10^{-3}$	
16	$1.41 \cdot 10^{-3}$	1.97	$1.37 \cdot 10^{-3}$	2.01	$4.07 \cdot 10^{-4}$	2.30
32	$3.54 \cdot 10^{-4}$	1.99	$3.43 \cdot 10^{-4}$	2.00	$9.47 \cdot 10^{-5}$	2.10
64	$8.85 \cdot 10^{-5}$	2.00	$8.55 \cdot 10^{-5}$	2.00	$2.32 \cdot 10^{-5}$	2.03
128	$2.21 \cdot 10^{-5}$	2.00	$2.14 \cdot 10^{-5}$	2.00	$5.76 \cdot 10^{-6}$	2.00
256	$5.53 \cdot 10^{-6}$	2.00	$5.34 \cdot 10^{-6}$	2.00	$1.44 \cdot 10^{-6}$	2.00
512	$1.38 \cdot 10^{-6}$	2.00	$1.33 \cdot 10^{-6}$	2.01	$3.60 \cdot 10^{-7}$	2.00
		equidistant triangular mesh, $k = 3$				
8	$1.04 \cdot 10^{-4}$		$1.48 \cdot 10^{-4}$		$1.52 \cdot 10^{-4}$	
16	$1.29 \cdot 10^{-5}$	3.01	$1.85 \cdot 10^{-5}$	3.00	$1.92 \cdot 10^{-5}$	2.98
32	$1.60 \cdot 10^{-6}$	3.01	$2.31 \cdot 10^{-6}$	3.00	$2.41 \cdot 10^{-6}$	2.99
64	$2.00 \cdot 10^{-7}$	3.00	$2.88 \cdot 10^{-7}$	3.00	$3.02 \cdot 10^{-7}$	3.00
128	$2.50 \cdot 10^{-8}$	3.00	$3.60 \cdot 10^{-8}$	3.00	$3.78 \cdot 10^{-8}$	3.00
256	$3.12 \cdot 10^{-9}$	3.00	$4.50 \cdot 10^{-9}$	3.00	$4.73 \cdot 10^{-9}$	3.00

5.2. Flow: Heterogeneous case

This example is taken from [9] and illustrates the case of highly discontinuous coefficients. We solve (1)-(4) in the unit square with $p = 1$ for $x = 0$, $p = 0$ for $x = 1$ and no flow boundary conditions for $y = 0$ and $y = 1$. The permeability field is defined on a 20×20 mesh and is shown in Fig. 1 on the left. In dark areas the permeability is $\boldsymbol{K} = 10^{-6} \cdot \boldsymbol{I}$, elsewhere it is $\boldsymbol{K} = \boldsymbol{I}$.

The unit square is discretized with $20 \times 20 \times 2$ triangular elements such that the permeability field is resolved with coarse grid elements. Finer grids are obtained through regular refinement. The right plot in Fig. 1 shows the flow field computed with degree $k = 3$ on the coarsest mesh.

Table V shows the convergence rates of the L^2 norm of $\boldsymbol{U}^{\mathrm{DG}} - \boldsymbol{U}^*$ for $k = 2$ and $k = 3$. The rates suggest that the unknown exact solution belongs to $H^s(\mathcal{E}_h)$ with $s \approx 1.7$.

5.3. Transport: Heterogeneous case

This example illustrates the advantage of the projected velocity proposed in this paper in connection with transport simulations using a DG space discretization. Eqs. (5)–(7) are solved

Table II. Full regularity model problem. Superconvergence of fluxes and jumps in pressure.

h^{-1}	$\sup_e \|(\{\boldsymbol{U}^{\mathrm{DG}}\} - \boldsymbol{u}) \cdot \boldsymbol{n}_e\|_{0,e}$				$\sup_e \|[P^{\mathrm{DG}}]\|_{0,e}$			
	$k = 2$	rate	$k = 3$	rate	$k = 2$	rate	$k = 3$	rate
				equidistant triangular mesh				
8	$9.98 \cdot 10^{-04}$		$2.67 \cdot 10^{-05}$		$8.65 \cdot 10^{-05}$		$1.58 \cdot 10^{-06}$	
16	$1.93 \cdot 10^{-04}$	2.37	$2.48 \cdot 10^{-06}$	3.43	$7.82 \cdot 10^{-06}$	3.47	$7.12 \cdot 10^{-08}$	4.47
32	$3.59 \cdot 10^{-05}$	2.43	$2.21 \cdot 10^{-07}$	3.49	$6.96 \cdot 10^{-07}$	3.49	$3.15 \cdot 10^{-09}$	4.50
64	$6.52 \cdot 10^{-06}$	2.46	$1.96 \cdot 10^{-08}$	3.50	$6.17 \cdot 10^{-08}$	3.50	$1.39 \cdot 10^{-10}$	4.50
128	$1.17 \cdot 10^{-06}$	2.48	$1.73 \cdot 10^{-09}$	3.50	$5.47 \cdot 10^{-09}$	3.50	$6.15 \cdot 10^{-12}$	4.50
256	$2.08 \cdot 10^{-07}$	2.49	$1.53 \cdot 10^{-10}$	3.50	$4.83 \cdot 10^{-10}$	3.50	$2.72 \cdot 10^{-13}$	4.50
				unstructured triangular mesh				
8	$1.05 \cdot 10^{-03}$		$3.46 \cdot 10^{-05}$		$8.68 \cdot 10^{-05}$		$1.85 \cdot 10^{-06}$	
16	$1.97 \cdot 10^{-04}$	2.41	$3.97 \cdot 10^{-06}$	3.12	$8.06 \cdot 10^{-06}$	3.43	$8.62 \cdot 10^{-08}$	4.42
32	$3.62 \cdot 10^{-05}$	2.44	$3.83 \cdot 10^{-07}$	3.37	$7.71 \cdot 10^{-07}$	3.39	$4.18 \cdot 10^{-09}$	4.37
64	$6.55 \cdot 10^{-06}$	2.47	$3.50 \cdot 10^{-08}$	3.45	$7.01 \cdot 10^{-08}$	3.46	$1.98 \cdot 10^{-10}$	4.40
128	$1.17 \cdot 10^{-06}$	2.48	$3.14 \cdot 10^{-09}$	3.48	$6.33 \cdot 10^{-09}$	3.47	$9.01 \cdot 10^{-12}$	4.46
256	$2.09 \cdot 10^{-07}$	2.48	$2.80 \cdot 10^{-10}$	3.49	$5.64 \cdot 10^{-10}$	3.49	$4.03 \cdot 10^{-13}$	4.48

Table III. Reentrant corner problem. Convergence rates for DG and projected velocities.

h^{-1}	$\|\boldsymbol{U}^{\mathrm{DG}} - \boldsymbol{u}\|_0$	rate	$\|\boldsymbol{U}^* - \boldsymbol{u}\|_0$	rate	$\|\boldsymbol{U}^{\mathrm{DG}} - \boldsymbol{U}^*\|_0$	rate
			triangular mesh, $k = 2$			
8	$1.01 \cdot 10^{-1}$		$1.09 \cdot 10^{-1}$		$2.93 \cdot 10^{-2}$	
16	$6.79 \cdot 10^{-2}$	0.573	$7.36 \cdot 10^{-2}$	0.567	$1.97 \cdot 10^{-2}$	0.573
32	$4.57 \cdot 10^{-2}$	0.571	$4.95 \cdot 10^{-2}$	0.572	$1.33 \cdot 10^{-2}$	0.567
64	$3.08 \cdot 10^{-2}$	0.569	$3.33 \cdot 10^{-2}$	0.572	$8.94 \cdot 10^{-3}$	0.573
128	$2.07 \cdot 10^{-2}$	0.573	$2.24 \cdot 10^{-2}$	0.572	$6.01 \cdot 10^{-3}$	0.573
256	$1.39 \cdot 10^{-2}$	0.575	$1.51 \cdot 10^{-2}$	0.567	$4.05 \cdot 10^{-3}$	0.569
			triangular mesh, $k = 3$			
8	$6.71 \cdot 10^{-2}$		$7.05 \cdot 10^{-2}$		$1.32 \cdot 10^{-2}$	
16	$4.51 \cdot 10^{-2}$	0.573	$4.74 \cdot 10^{-2}$	0.573	$8.83 \cdot 10^{-3}$	0.580
32	$3.04 \cdot 10^{-2}$	0.569	$3.19 \cdot 10^{-2}$	0.571	$5.94 \cdot 10^{-3}$	0.572
64	$2.04 \cdot 10^{-2}$	0.576	$2.15 \cdot 10^{-2}$	0.569	$3.99 \cdot 10^{-3}$	0.574
128	$1.38 \cdot 10^{-2}$	0.564	$1.44 \cdot 10^{-2}$	0.578	$2.69 \cdot 10^{-3}$	0.569

Table IV. Reentrant corner problem. Convergence of fluxes and jumps in pressure at interior edges.

h^{-1}	$\sup_e \|(\{\boldsymbol{U}^{\mathrm{DG}}\} - \boldsymbol{u}) \cdot \boldsymbol{n}_e\|_{0,e}$				$\sup_e \|[P^{\mathrm{DG}}]\|_{0,e}$			
	$k = 2$	rate	$k = 3$	rate	$k = 2$	rate	$k = 3$	rate
8	$3.61 \cdot 10^{-1}$		$2.89 \cdot 10^{-1}$		$8.29 \cdot 10^{-3}$		$4.59 \cdot 10^{-3}$	
16	$3.43 \cdot 10^{-1}$	0.074	$2.75 \cdot 10^{-1}$	0.072	$3.95 \cdot 10^{-3}$	1.070	$2.19 \cdot 10^{-3}$	1.068
32	$3.27 \cdot 10^{-1}$	0.069	$2.62 \cdot 10^{-1}$	0.070	$1.88 \cdot 10^{-3}$	1.071	$1.04 \cdot 10^{-3}$	1.074
64	$3.11 \cdot 10^{-1}$	0.072	$2.49 \cdot 10^{-1}$	0.073	$8.95 \cdot 10^{-4}$	1.071	$4.95 \cdot 10^{-4}$	1.071
128	$2.96 \cdot 10^{-1}$	0.071	$2.37 \cdot 10^{-1}$	0.071	$4.26 \cdot 10^{-4}$	1.071	$2.36 \cdot 10^{-4}$	1.069
256	$2.82 \cdot 10^{-1}$	0.070			$2.03 \cdot 10^{-4}$	1.070		
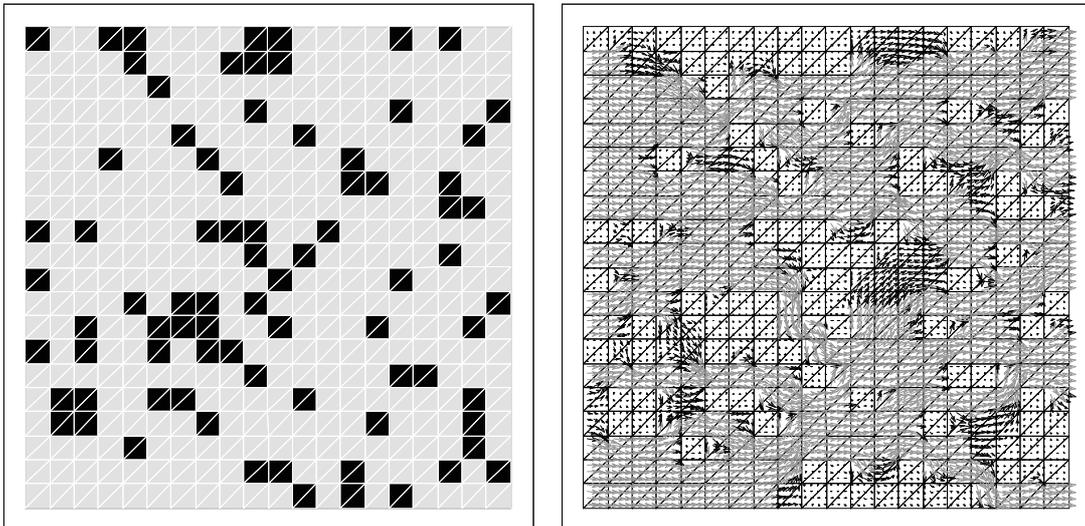
Figure 1. Permeability and flow field for the discontinuous coefficient example computed with DG(3). Permeability 1 shown in light gray and 10^{-6} in black. Vectors not drawn to scale are indicated by gray color in the vector plot.

Table V. Heterogeneous flow problem for triangular mesh

	$k = 2$		$k = 3$	
h^{-1}	$\|\boldsymbol{U}^{\mathrm{DG}} - \boldsymbol{U}^*\|_0$	rate	$\|\boldsymbol{U}^{\mathrm{DG}} - \boldsymbol{U}^*\|_0$	rate
20	$4.68 \cdot 10^{-2}$		$2.43 \cdot 10^{-2}$	
40	$2.82 \cdot 10^{-2}$	0.73	$1.70 \cdot 10^{-2}$	0.52
80	$1.79 \cdot 10^{-2}$	0.66	$1.05 \cdot 10^{-2}$	0.70
160	$1.12 \cdot 10^{-2}$	0.68	$6.58 \cdot 10^{-3}$	0.67
320	$7.01 \cdot 10^{-3}$	0.68		

Table VI. Summary of convergence rates for pressure approximations of degree k.

error	theoretical rate	numerical rate	superconvergence
$\|\boldsymbol{U}^{\mathrm{DG}} - \mathbf{u}\|_0$	h^k	h^k	
$\|\boldsymbol{U}^* - \mathbf{u}\|_0$	h^k	h^k	
$\sup_e \|\{\boldsymbol{U}^{\mathrm{DG}}\} - \mathbf{u}\|_{0,e}$	$h^{k-1/2}$	$h^{k+1/2}$	$\checkmark$
$\sup_e \|\boldsymbol{U}^* - \mathbf{u}\|_{0,e}$	$h^{k-1/2}$	$h^{k+1/2}$	$\checkmark$
$\sup_e \|[P^{\mathrm{DG}}]\|_{0_e}$	$h^{k-1/2}$	$h^{k+3/2}$	$\checkmark$

in the flow field shown in Fig. 2 generated by a setup identical to that in the previous section except that the permeability field has a single low permeability zone.

Parameters for eq. (5) are $\psi = 1, R(S) = 0$ and $D = 0$ (pure convection). Boundary conditions are $S = 1$ at $x = 0$, no flow at $y = 0$ and $y = 1$ and outflow at $x = 1$. Initial condition is $S = 0$ in Ω.

The problem is solved by a DG space discretization as developed in [19] using DG(1) elements and implicit Euler discretization in time. The flow field is computed with DG(2). The approximate solutions are shown at the final simulation time $T = 20$. Since $|\boldsymbol{u}| \approx 1$ and the domain has a diameter of order 1 the solution is expected to be $S = 1$ in the highly permeable region and $S = 0$ in the low permeably region. The plot on the left in Fig. 3 shows the concentration obtained with a DG flow and transport calculation. The solution shows an overshoot of 33%. The right plot in Fig. 3 shows the solution that is obtained by replacing the DG velocity field with the projected velocity $\boldsymbol{U}^*$. The solution does not show any over- or undershoots. The reason for the oscillations obtained with the DG velocity field is that the averaged normal flux on element edges $\{\boldsymbol{U}^{\mathrm{DG}}\} \cdot \boldsymbol{n}_e$ is not continuous. This is visualized in Fig. 4. The figure shows the flow field in two neighbouring triangles. Clearly, the *normal* velocity is not the same on both sides of the 45 degree edge near the lower left corner of the plot on the left which is obtained from the DG velocity. The right plot shows the projected velocity field with continuous normal component.

It should be noted that both solutions have been obtained without using slope limiters. Clearly, a slope limiter is able to remove the oscillations obtained with the DG velocity since the solution has the correct cell averages. However, a slope limiter should not be necessary in the problem shown here.

6. Conclusion

In this paper we have introduced and analyzed a projection of the DG approximations that preserve the local mass conservation property. The projected velocities have the additional property of continuous normal component. Both theoretical and numerical convergence rates have been obtained; they are summarized in Table VI for a regular solution. Superconvergence properties of the DG methods are shown. Finally, the H(div) projection has been applied to complicated flow and transport problem and the resulting solution is shown to be more accurate.
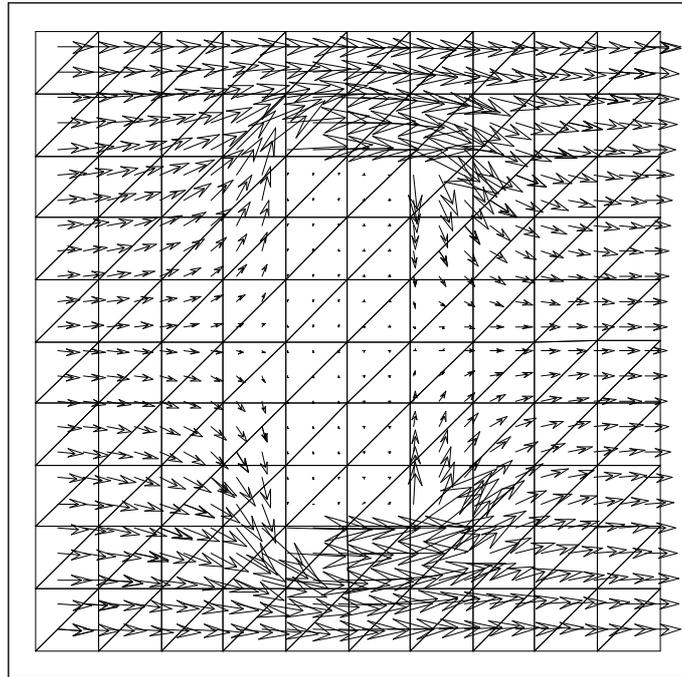
Figure 2. Flow field used for the transport simulation.
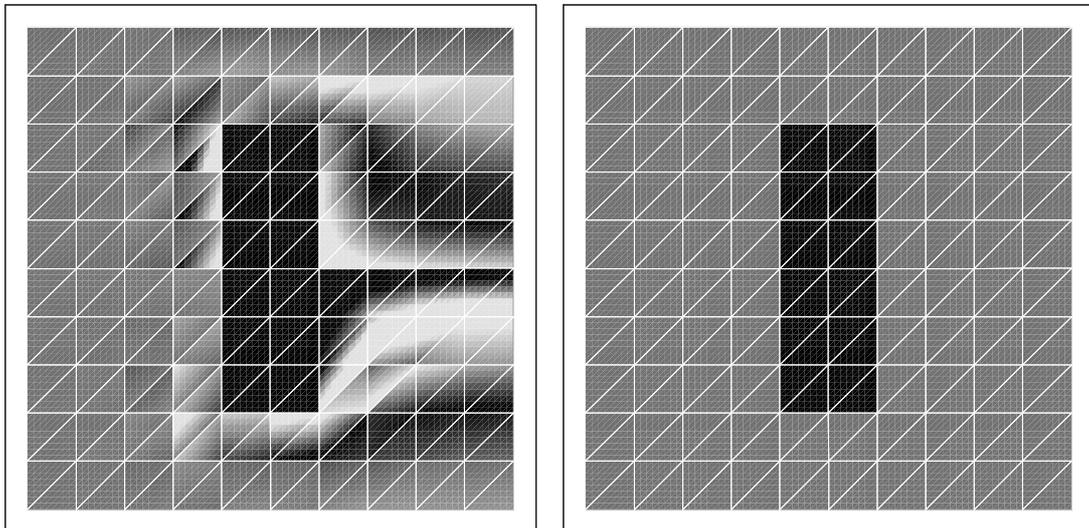
Figure 3. Stationary solution of a transport calculation. DG flowfield left and projected flow field right. Medium gray means $S = 1.0$, $S < 0.9$ is shown black and $S > 1.1$ is white. Maximum overshoot in left plot is 1.33.
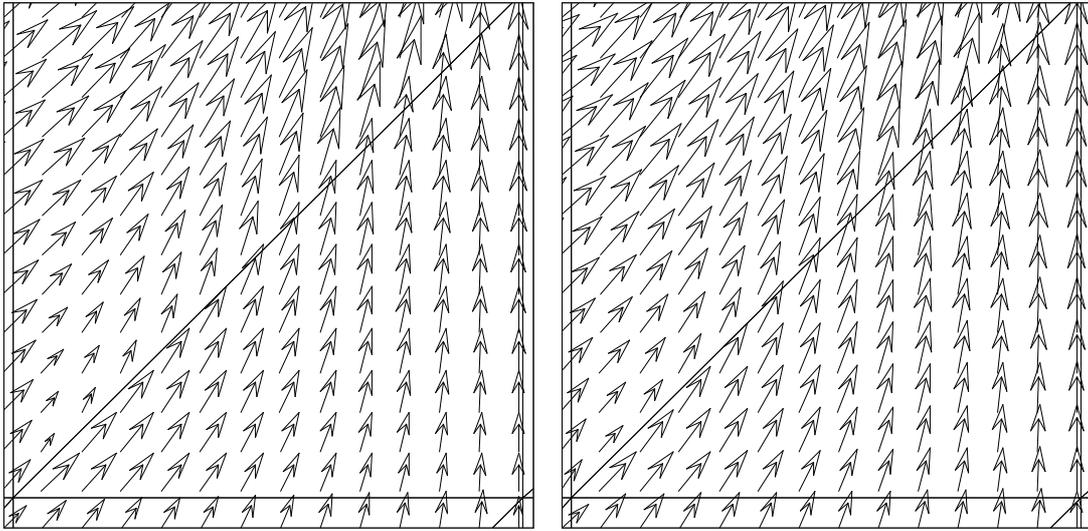
Figure 4. Comparison of DG (left) and projected (right) flow field.

REFERENCES

1. Adams RA. *Sobolev Spaces.* Academic Press, New York, 1975.
2. Aizinger V, Dawson C, Cockburn B, Castillo P. The local discontinuous Galerkin method for contaminant transport. *Advances in Water Resources* 2001. **24**:73–87.
3. Arnold DA. An interior penalty finite element method with discontinuous elements *SIAM Journal on Numerical Analysis* 1982; **19**:742–760.
4. Arnold DA, Brezzi F, Cockburn B, Marini L. Unified analysis of discontinuous Galerkin methods for elliptic problems. *SIAM Journal on Numerical Analysis* 2002; **39**(5):1749–1779.
5. Brezzi F, Douglas J, Marini LD. Two families of mixed finite elements for second order elliptic problems. *Numerische Mathematik* 1985; **47**:217–235.
6. Ciarlet P. *The finite element methods for elliptic problems.* North-Holland, Amsterdam, 1978.
7. Cockburn B., Karniadakis G, and Shu C. The development of discontinuous Galerkin methods. In *Discontinuous Galerkin methods. Theory, computation and applications. Lecture Notes in Computational Science and Engineering.* Cockburn B, Lin S, Shu CW (eds.). Springer-Verlag; 2000. **11**:3–50.
8. Cockburn B., Shu CW. The local discontinuous Galerkin finite element method for convection-diffusion systems. *SIAM Journal on Numerical Analysis* 1998; **35**:2440–2463.
9. Durlofsky LJ. Accuracy of mixed and control volume finite element approximations to Darcy velocity and related quantities. *Water Resources Research* 1994; **30**(4):965–973.
10. Grisvard P. *Elliptic problems in nonsmooth domains.* Pitman Monographs and Studies in Mathematics 24, Pitman, Boston, MA 1985.
11. Houston P, Schwab C, Suli E. Discontinuous hp-finite element methods for advection-diffusion problems. *Research report No. 2000-07*, 2000.
12. Lesaint P, Raviart PA. On a finite element method for solving the neutron transport equation. In *Mathematical Aspects of Finite Element Methods in Partial Differential Equations,* deBoor CA (ed). Academic Press, 1974; 89–123.
13. Lions JL, Magenes E. *Problèmes aux Limites non Homogènes et Applications, I.* Dunod, Paris, 1968.
14. Lions JL. *Quelques méthodes de résolution des problèmes aux limites non linéaires.* Dunod, Paris, 1969.
15. Oden JT, Babuška I, Baumann CE, A discontinous hp finite element method for diffusion problems. *Journal of Computational Physics* 1998; **146**:491–519.
16. Reed W, Hill T. Triangular mesh methods for the neutron transport equation. *Technical report, Los Alamos Scientific Laboratory*; 1973.
17. Rivière B, Wheeler MF, Girault V. Improved energy estimates for interior penalty, constrained and

Copyright © 2000 John Wiley & Sons, Ltd.

Prepared using fldauth.cls

Int. J. Numer. Meth. Fluids 2000; **00**:1–6

discontinuous Galerkin methods for elliptic problems. Part I. *Computational Geosciences* 1999; **3**:337–360.

18. Rivière B, Wheeler MF, Girault V. A priori error estimates for finite element emthods based on discontinuous approximation spaces for elliptic problems. *SIAM Journal on Numerical Analysis* 2001; **39**(3):902–931.

19. Rivière B, Wheeler MF. Nonconforming methods for transport with nonlinear reaction. In *Fluid Flow and Transport in Porous Media: Mathematical and Numerical* Chen Z, Ewing RE (eds). American Mathematical Society, 2002; **295**:421–432.

20. Rivière B., Wheeler MF, Banaś K. Part II. Discontinuous Galerkin method applied to a single phase flow in porous media. *Computational Geosciences* 2000. **4**:337–349.

21. Wheeler MF. An elliptic collocation-finite element method with interior penalties. *SIAM Journal on Numerical Analysis* 1978; **15**(1):152–161.